ACS APPLIED MATERIALS & INTERFACES

Research Article

www.acsami.org

Solution-Processed $CoFe_2O_4$ Nanoparticles on 3D Carbon Fiber Papers for Durable Oxygen Evolution Reaction

Alireza Kargar,[†] Serdar Yavuz,[‡,§] Tae Kyoung Kim,[‡,§] Chin-Hung Liu,[‡,§] Cihan Kuru,[‡,§] Cyrus S. Rustomji,[‡,§] Sungho Jin,[*,‡,§] and Prabhakar R. Bandaru[*,†,‡,§]

[†]Department of Electrical and Computer Engineering, University of California—San Diego, 9500 Gilman Drive, La Jolla, California 92093, United States

[‡]Materials Science and Engineering Program, University of California—San Diego, 9500 Gilman Drive, La Jolla, California 92093, United States

[§]Department of Mechanical and Aerospace Engineering, University of California—San Diego, 9500 Gilman Drive, La Jolla, California 92093, United States

Supporting Information

ABSTRACT: We report $CoFe_2O_4$ nanoparticles (NPs) synthesized using a facile hydrothermal growth and their attachment on 3D carbon fiber papers (CFPs) for efficient and durable oxygen evolution reaction (OER). The CFPs covered with $CoFe_2O_4$ NPs show orders of magnitude higher OER performance than bare CFP due to high activity of $CoFe_2O_4$ NPs, leading to a small overpotential of 378 mV to get a current density of 10 mA/cm^2. Significantly, the $CoFe_2O_4$ NPs-on-CFP electrodes exhibit remarkably long stability evaluated by continuous cycling (over 15 h) and operation with a high current density at a fixed potential (over 40 h) without any morphological change and with preservation of all materials within the electrode. Furthermore, the $CoFe_2O_4$ NPs-on-CFP electrodes also exhibit hydrogen evolution reaction (HER) performance, which is considerably higher than that of bare CFP, acting as a bifunctional electrocatalyst. The achieved results show promising potential for efficient, cost-effective, and durable hydrogen generation at large scales using earth-abundant materials and cheap fabrication processes.

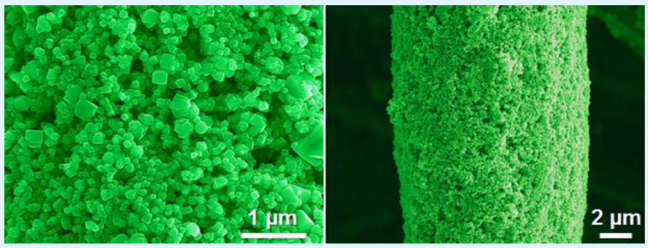

KEYWORDS: *$CoFe_2O_4$, nanoparticles (NPs), carbon fiber paper (CFP), water splitting, oxygen evolution reaction (OER)*

1. INTRODUCTION

Water splitting for hydrogen fuel generation, either using electricity or sunlight as a driving force, is considered to be a viable pathway to fulfill the demanding energy requirements.[1−5] Catalysts play a significant role in water splitting reactions, hydrogen or oxygen evolution reaction (HER or OER), to facilitate efficient gas evolution. Between the HER and OER, it is more difficult to achieve efficient and stable gas evolution in the OER, because the OER is kinetically slow and needs four electron transfer steps, compared to two electron transfer steps required for the HER. Therefore, the OER typically results in a considerable efficiency loss in the water splitting process.[6−9]

Among different OER catalysts, cobalt-based catalysts have attracted considerable attention due to their abundance, low cost, competitive OER activity to precious metal oxides, etc.[10−18] Cobalt phosphate (Co—Pi) has been demonstrated as a highly active OER catalyst working in neutral water by Nocera's group.[10,11] Liang et al. have shown Co_3O_4/graphene hybrid as a very active OER catalyst which can also be used as an efficient oxygen reduction reaction (ORR) catalyst.[14] The cobalt-based catalysts can also be applied as OER catalyst/cocatalyst on the surface of semiconductor absorbers to simultaneously improve their OER performance and stabilize them.[19−21] McCrory et al. have reported $CoFeO_x$ as a promising OER electrocatalyst in 1 M NaOH solution with a low overpotential comparable to IrO_x but with much higher stability.[15] Particularly, $CoFe_2O_4$ (cobalt ferrite) can be a promising electrocatalyst due to its unique properties.[22−25] On the other hand, the size and morphology of the catalysts are crucial to achieve efficient electrochemical or photoelectrochemical (PEC) water splitting and hydrogen production. For the electrochemical hydrogen generation, developing catalysts on high-surface-area substrates is very useful in order to achieve high-efficiency gas evolution, while for the PEC hydrogen production, developing small nanoparticles (NPs) to attach on the surface of semiconductor absorbers is necessary. Besides catalyst performance, long time catalyst electrode stability is a key parameter to pave the way for practical hydrogen generation. Moreover, facile and scalable catalyst synthesis is also of significant importance in facilitating practical applications.

Received: May 16, 2015
Accepted: July 28, 2015
Published: July 28, 2015

DOI: 10.1021/acsami.5b04270
ACS Appl. Mater. Interfaces 2015, 7, 17851−17856

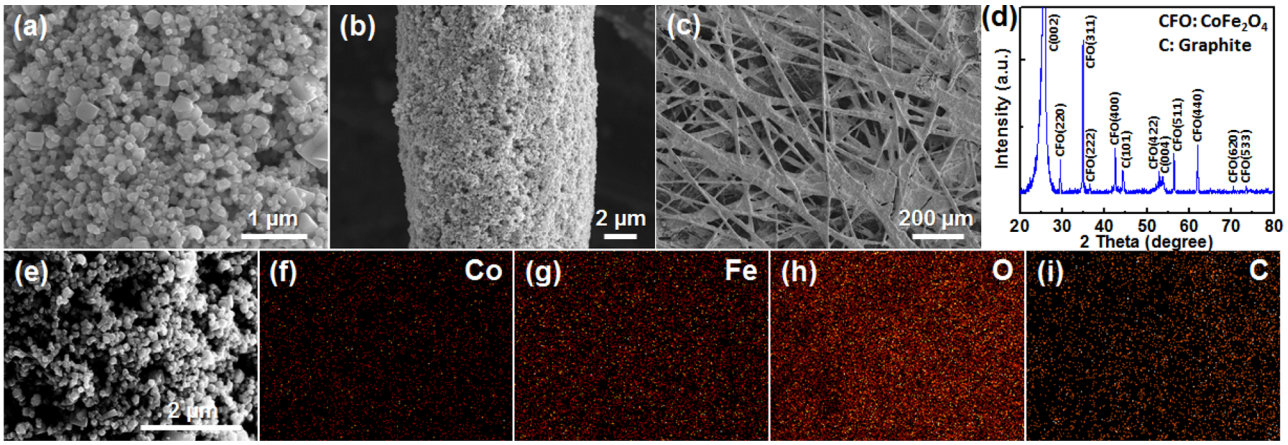

Figure 1. (a–c) SEM images (different magnification) and (d) XRD pattern of $CoFe_2O_4$ NPs on CFP. (e–i) Elemental mapping analysis of $CoFe_2O_4$ NPs on CFP; (e) SEM image of spot used for the elemental mapping, (f) Co map, (g) Fe map, (h) O map, and (i) C map. The scale bar for (f–i) is the same as that in (e).

In this paper, we present $CoFe_2O_4$ NPs synthesized by a simple hydrothermal growth method and their attachment using spin coating on 3D carbon fiber papers (CFPs) for efficient and durable OER. The $CoFe_2O_4$ NPs-on-CFP electrode shows significantly enhanced OER performance compared to bare CFP due to high activity of the $CoFe_2O_4$ NPs. Noticeably, the $CoFe_2O_4$ NPs-on-CFP electrodes show long-term stability over continuous cycling (over 15 h) and operation with a high current density at a fixed potential (over 40 h) without any morphological and compositional changes. The $CoFe_2O_4$ NPs on CFP are characterized in detail before and after long-term stability tests. Furthermore, the $CoFe_2O_4$ NPs-on-CFP electrodes also show HER performance, which is substantially higher than that of bare CFP, acting as a bifunctional catalyst.

2. EXPERIMENTAL SECTION

2.1. Synthesis of $CoFe_2O_4$ NPs. Cobalt chloride ($CoCl_2{\cdot}6H_2O$) and iron chloride ($FeCl_2{\cdot}4H_2O$) were purchased from Alfa Aesar and utilized as precursors. One M of cobalt chloride aqueous solution and 1 M of iron chloride aqueous solution were mixed in a volume ratio of 1 to 2. The coprecipitation in hydroxide form of cobalt and iron was induced by adding 10 M NaOH aqueous solution gradually in the process of vigorous stirring until pH of the coprecipitated solution reached a value of 11.5. The deionized (DI) water resistivity was 18.2 MΩ-cm for all the prepared solutions. The as-prepared solution with a high pH was transferred into a 45 mL sealed Teflon autoclave and subjected to hydrothermal growth for 20 h at a temperature of 150 °C by putting the filled autoclave in a regular oven. The remaining precursor and reaction byproducts were removed with repeated washing in DI water followed by centrifuging, after which freeze-drying was employed for 24 h to dry the centrifuged particles.

2.2. Fabrication of $CoFe_2O_4$ NPs Electrodes. The electrodes were prepared by spin coating of a $CoFe_2O_4$ solution onto the CFPs (FuelCellStore) or fluorine-doped tin oxide (FTO) substrates. The 0.66 wt % $CoFe_2O_4$ solution for spin coating was prepared in methanol followed by 30 min sonication to have a uniform dispersion of NPs. The prepared solution also underwent 15 min sonication right before the spin coating process in order to have a similar uniform concentration. The CFPs were subjected to 5 min O_2 plasma before the spin coating. Note that the tested bare CFPs were also subjected to 5 min of O_2 plasma for better comparison with the $CoFe_2O_4$-coated CFPs which were made using the plasma-treated CFPs. The O_2 plasma treatment before spin coating did not change the morphology of fibers (see Supporting Information Figure S1). The FTO substrates were consecutively cleaned by sonication for 5 min in acetone, isopropanol (IPA), and DI water, and finally rinsed with DI water and dried with N_2 gas. The CFP or FTO substrate was fixed on a clean glass slide as supporting substrate using a Kapton tape at one edge of substrate which also provided the contact area to attach a wire for measurement. To have a uniform distribution of $CoFe_2O_4$ NPs, three steps of spin coating were carried out with an optimized speed (rpm) and time for each step, including (i) 500 rpm for 10 s, (ii) 1500 rpm for 20 s, and (iii) 4000 rpm for 60 s. The three-step spin coating was performed several times (16 times) to get as uniform a coating of the $CoFe_2O_4$ NPs on the CFP substrate as possible, which will be shown in the following. The mass loading of $CoFe_2O_4$ NPs on CFP was estimated to be ∼1.031 mg/cm^2 using a microbalance. The coating of NPs on the FTO substrate was also performed using the optimized three steps but with 6 times spin coating in which the NPs coating was not uniform due to aggregation of NPs. For the $CoFe_2O_4$ NPs mixed with carbon (TIMCAL, Supper C65), 0.66 wt % solution of $CoFe_2O_4$ and carbon powder (using similar amount for each one) was prepared in methanol and spin-coated on the FTO substrate using similar procedure mentioned above. For the RuO_2 NPs on CFP samples, a 0.66 wt % solution of commercial RuO_2 (Sigma-Aldrich) was prepared in ethanol followed by 30 min sonication to have a uniform NP distribution. After that, the solution was spin-coated on the plasma-treated CFPs several times to get as uniform as possible coating of the RuO_2 NPs on CFP. Coated Cu wire was then attached onto the CFP or FTO substrate using a conductive epoxy (CW2400) cured overnight at room temperature, which provides an ohmic contact. The contact area was then sealed by the Hysol 1C epoxy, which was cured/dried over a long time, to prevent exposure to the electrolyte.

2.3. Characterization. The sample morphologies were examined on a Philips XL30 field-emission environmental scanning electron microscope (ESEM) at an accelerating voltage of 10.0 kV. Energy-dispersive X-ray spectroscopy (EDS) and elemental mapping analyses were used to examine the materials composition. Crystal structures of the $CoFe_2O_4$ NPs on CFPs were characterized using X-ray diffraction (XRD) by a Bruker D2 Phaser X-ray diffractometer with Cu K_α (λ = 0.154 nm) as the radiation source.

2.4. Electrochemical Measurements. Electrochemical measurements were performed in a ∼80 mL aqueous solution of 1 M NaOH (Sigma-Aldrich) with a pH of 13.97 (DI water resistivity, 18.2 MΩ-cm) using a homemade setup with a Teflon beaker and three electrodes configuration, including sample as working electrode (WE), Pt foil as counter electrode (CE), and Hg/HgO (1 M NaOH) as reference electrode (RE). The electrochemical measurements were collected using a potentiostat (Digi-Ivy, DY2300). A scan rate of 20 mV/s was employed for all the current density measurements. During the electrochemical measurements, a mild agitation was employed, and the electrolyte was constantly purged with a small flow of N_2 gas. Also, before the start of each electrochemical measurement, the electrolyte

DOI: 10.1021/acsami.5b04270
ACS Appl. Mater. Interfaces 2015, 7, 17851–17856

was purged with N_2 gas with higher flow than that used during the measurements. Note that for the evaluation of sample for both HER and OER performances, we did not use any gas purging during the test or before the test, which will be discussed further in the following. The external biasing potentials here are versus Hg/HgO RE or reversible hydrogen electrode (RHE). The biasing potentials versus Hg/HgO RE ($E_{Hg/Hgo}$) were converted to the potentials versus RHE (E_{RHE}) using the Nernst equation as follows:

$$E_{RHE} = E_{Hg/HgO} + 0.059 \times pH + E^0_{Hg/HgO}\ (V) \quad (1)$$

where pH is the electrolyte pH and $E^0_{Hg/HgO}$ = 0.098 V versus normal hydrogen electrode (NHE) at 25 °C for the Hg/HgO/1 M NaOH (CH Instruments, Inc.). The OER overpotential (η) was calculated using the below equation:

$$\eta = E_{Hg/HgO} - E^0(O_2/H_2O)\ (V) \quad (2)$$

where $E^0(O_2/H_2O)$ is the thermodynamic potential for water oxidation (the OER) relative to Hg/HgO at pH = 13.97, which was calculated to be 0.307 V using

$$E^0(O_2/H_2O) = 1.23 - 0.059 \times pH - E^0_{Hg/HgO}\ (V) \quad (3)$$

The overpotential for the HER was also calculated using eq 2 considering $E^0(H^+/H_2)$ instead of $E^0(O_2/H_2O)$. $E^0(H^+/H_2)$ is the thermodynamic potential for water reduction (the HER) relative to Hg/HgO at pH = 13.97, which was calculated to be −0.922 V using the following:

$$E^0(H^+/H_2) = -0.059 \times pH - E^0_{Hg/HgO}\ (V) \quad (4)$$

All the potentials and plots reported here are without considering any *iR* correction. The current densities here are calculated using geometric surface areas.

3. RESULTS AND DISCUSSION

Figure 1a–c shows scanning electron microscopy (SEM) images of $CoFe_2O_4$ NPs spin-coated on the CFP. The coating of $CoFe_2O_4$ NPs on carbon fibers in the CFP is relatively uniform and dense, as shown in Figure 1, parts b and c. SEM images of different parts of samples showed that most of the carbon fibers were uniformly coated with $CoFe_2O_4$ NPs. Note that there are some residues between some fibers which are due to the purchased CFP (see Figure S1). The XRD pattern of $CoFe_2O_4$ NPs on CFP (Figure 1d) exhibits well-matched peaks with standard $CoFe_2O_4$ reference (JCPDS card no. 00-022-1086). The graphite peaks from the CFP can also be seen in the XRD pattern. The average grain size of $CoFe_2O_4$ NPs using the Scherrer equation and XRD data was estimated to be 60 nm. The average NPs size calculated using the SEM image (see Figure S2) is 69 nm which is comparable to the estimated average size from the Scherrer equation. The elemental mapping analysis shown in Figure 1e–i confirms the material composition of $CoFe_2O_4$ NPs on CFP.

The OER performance of $CoFe_2O_4$ NPs on CFP is shown in Figure 2a exhibiting a current density of 10 mA/cm^2 at an overpotential (η) of 378 mV. The achieved overpotential is consistent with that reported for the $CoFeO_x$ catalyst in 1 M NaOH.[15] The bare CFP shows a current density of 8 mA/cm^2 at η = 886 mV, demonstrating the remarkable catalytic effect of $CoFe_2O_4$ NPs. The $CoFe_2O_4$ NPs spin-coated on FTO substrate also show much higher OER performance than bare FTO substrate (see Figure S3), confirming the high OER performance of $CoFe_2O_4$ NPs. The $CoFe_2O_4$ NPs mixed with carbon and spin-coated on FTO exhibit higher performance compared to the bare $CoFe_2O_4$ NPs on FTO (see Figure S4), indicating that there may be a synergetic effect between

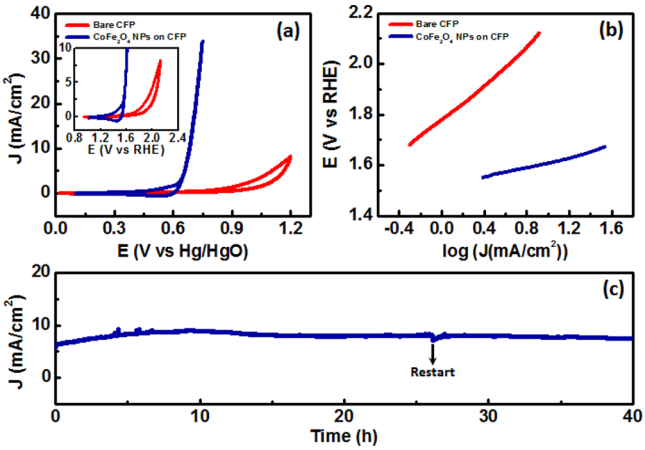

Figure 2. (a) Cyclic voltammetry (CV) measurement of $CoFe_2O_4$ NPs on CFP and bare CFP recorded at a scan rate of 20 mV/s in 1 M NaOH. Inset shows the zoomed-in current density versus RHE. (b) Tafel plot of corresponding samples in (a). (c) Current density versus time of $CoFe_2O_4$ NPs on CFP measured at a fixed potential of 0.675 V versus Hg/HgO RE in 1 M NaOH. The plots are without any *iR* correction.

$CoFe_2O_4$ NPs and carbon substrate from the CFP contributing to the enhanced performance.[14] The $CoFe_2O_4$ NPs on CFP do not show any hysteresis feature at high biasing potentials, while there is a small hysteresis at low biasing potentials (see Figure 2a), which reaches a very small value over cycling (see Figure 3a and its inset). The $CoFe_2O_4$ NPs-on-CFP electrode shows a Tafel slope of ∼73 mV/dec, much lower than that of bare CFP which is ∼333 mV/dec (Figure 2b). The $CoFe_2O_4$ NPs on CFP exhibit a little lower performance than the commercial RuO_2 NPs on CFP with almost similar mass loading and uniformity (see Figures S5 and S6). The OER performance of the $CoFe_2O_4$ NPs may be further enhanced using electrochemical lithium tuning.[9] The developed catalyst structure can also easily be used for other metal oxide NPs catalysts to further reduce the overpotential and boost the performance. It is hard to directly compare the obtained OER results with that of the reported $CoFe_2O_4$ NPs-on-glassy-carbon, $CoFe_2O_4$/biocarbon nanocomposite, and $CoFe_2O_4$/graphene nanohybrid electrocatalysts as the solution concentration, catalyst loading, and electrode preparation are different.[23−25] The $CoFe_2O_4$ NPs on CFP with a mass loading of ∼1.031 mg/cm^2 shows higher performance (higher current density) in 1 M NaOH compared to that of the $CoFe_2O_4$/graphene nanohybrid catalyst with a loading of 1.006 mg/cm^2 in 0.1 M KOH.[24] The $CoFe_2O_4$ NPs-on-CFP electrode with a loading of ∼1.031 mg/cm^2 exhibits lower overpotential of 10 mA/cm^2 in 1 M NaOH than that of the reported crystalline $CoFe_2O_4$ NPs on glassy carbon with a loading of 0.051 mg/cm^2 in 0.1 KOH (η = 560 mV).[23] More importantly, the $CoFe_2O_4$ NPs-on-CFP electrode shows much longer investigated stability in 1 M NaOH, which will be shown in the following, compared to the $CoFe_2O_4$ NPs-on-glassy-carbon,[23] $CoFe_2O_4$/biocarbon nanocomposite,[25] and $CoFe_2O_4$/graphene nanohybrid[24] catalysts in 0.1 M KOH.

The $CoFe_2O_4$ NPs-on-CFP sample exhibits a long stability of at least 40 h at a high current density without any morphological or materials changes (see Figure 2c and S3). The electrode stability is also investigated by long cycling performance with detailed post characterization, which will be discussed in the following. As shown in Figure 2c, the current density first increases a little and then reaches a saturation state

DOI: 10.1021/acsami.5b04270
ACS Appl. Mater. Interfaces 2015, 7, 17851−17856

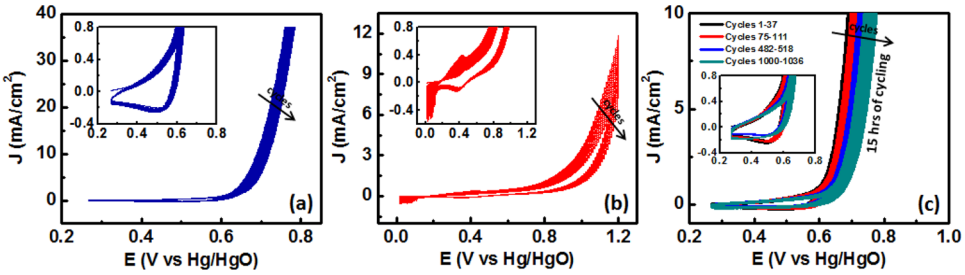

Figure 3. Consecutive cyclic voltammetry (CV) scans of (a) $CoFe_2O_4$ NPs on CFP (37 cycles) and (b) bare CFP (27 cycles) collected at a scan rate of 20 mV/s in 1 M NaOH. (c) Long cycling performance of over 1000 cycles, taking over 15 h, of $CoFe_2O_4$ NPs on CFP recorded at a scan rate of 20 mV/s in 1 M NaOH. Insets in (a–c) are the zoomed-in current density of the corresponding plots. Arrows in (a–c) show the direction of increase for the cycle number. The plots are without any *iR* correction.

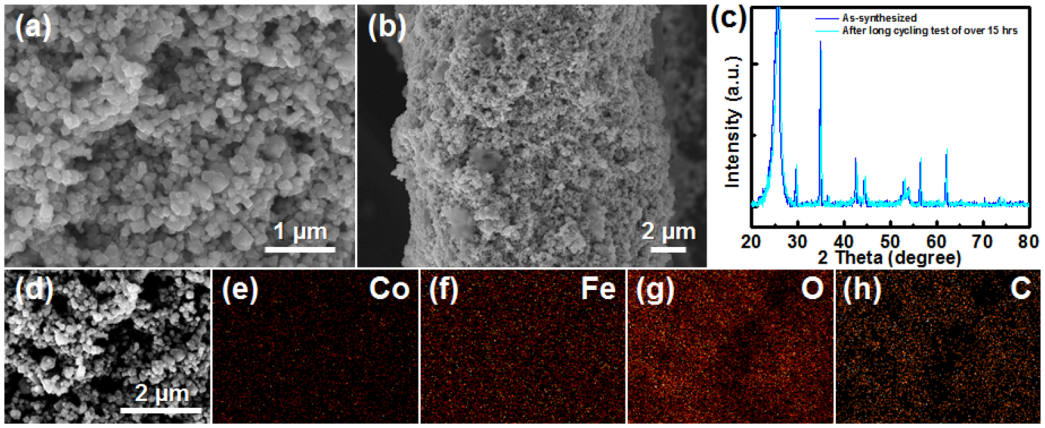

Figure 4. Characterization of $CoFe_2O_4$ NPs on CFP after long cycling test of over 15 h (shown in Figure 3c): (a,b) SEM images with different magnification, (c) XRD pattern along with the XRD of as-synthesized $CoFe_2O_4$ NPs on CFP for comparison, and (d–h) elemental mapping analysis of $CoFe_2O_4$ NPs on CFP; (d) SEM image of spot used for the elemental mapping, (e) Co map, (f) Fe map, (g) O map, and (h) C map. The scale bar for (e–h) is the same as that in (d).

with minimal change over long time. No specific conditioning test before the long stability test was performed. After testing the sample for CV measurements and a short test of current density versus time, the sample was washed with DI water, the bubbles were removed from the electrolyte, and afterward the long stability test was run. To be certain about the performance and continuous operation, the measurement was stopped after 27.77 h and ran again (indicated in Figure 2c) without any change in the measurement setup and sample. As shown in Figure 2c, shortly after restarting, the current density reached saturation at the same current density as before stopping the measurement. To validate the morphology and materials preservation after such a long stability test, SEM imaging was performed on the sample (see Figure S7), showing that there is no noticeable morphological or material changes either in the $CoFe_2O_4$ NPs or in the carbon fibers. The achieved long-term stability of over 40 h is much longer than that investigated for the $CoFe_2O_4$/biocarbon nanocomposites (<13 h),[25] $CoFe_2O_4$/graphene nanohybrids (<13 h),[24] and $CoFe_2O_4$ NPs on glassy carbon (30 min).[23] As the material itself is stable under such a high current density and alkaline electrolyte, we believe that much longer stability can be achieved.

The cycling performance of $CoFe_2O_4$ NPs-on-CFP electrode and bare CFP is shown in Figure 3, parts a and b. Note that the data in Figure 3 was measured on another sample fabricated similarly to that shown in Figure 2. The overpotential of 10 mA/cm^2 for the $CoFe_2O_4$ NPs on CFP does not change over 37 consecutive CV cycles (see Figure 3a and its inset). Moreover, there is no hysteresis feature at high biasing potentials in all 37 CV scans (similar observation was seen for the $CoFe_2O_4$ NPs on the FTO substrate (see Figure S3)). At low biasing potentials, there is only a very small hysteresis for all CV scans (Figure 3a inset). In contrast, the bare CFP shows hysteresis feature at both low and high biasing potentials with an increase in the overpotential over cycling (see Figure 3b and its inset). Also the high current densities at high biasing potentials do not change significantly for the $CoFe_2O_4$ NPs-on-CFP electrode while they decrease for the bare CFP over cycling. This may be an indication of the fact that the CFP and its surface may change in the NaOH solution and decoration of NPs helps the surface passivation.

The stability of $CoFe_2O_4$ NPs-on-CFP electrode was further investigated by a long cycling test of over 1000 cycles using a slow scan rate of 20 mV/s and under continuous operation (measurement time was over 15 h) without any change in measurement setup and sample (Figure 3c). Up to over 100 cycles, there is no significant change in the overpotential at a current density of 10 mA/cm^2. Over larger number cycles, around 500 and 1000, there is only a very small change in the overpotential at a current density of 10 mA/cm^2 (overpotential difference between cycle 1 and cycle 1036 is about 100 mV (see Figure 3c and its inset)). Moreover, there is no hysteresis feature at high biasing potentials (Figure 3c) and at low biasing potentials, the hysteresis remains very small with negligible changes (Figure 3c inset). Over longer cycles of 500 and 1000, the current density at high biasing potentials starts to reduce

DOI: 10.1021/acsami.5b04270
ACS Appl. Mater. Interfaces 2015, 7, 17851–17856

which can be possibly due to the large amount of bubbles formed during the experiment. We performed 28 repeated tests of 37 consecutive cycles to get a total of 1036 cycles due to the limitation of our potentiostat. Thus, this can be another reason for the current density reduction at high biasing potentials. However, the current density at high biasing potentials is not of particular interest for hydrogen production because the main purpose is to build full systems to run overall water splitting, which requires active electrodes with high current density at low biasing potentials.

It is useful to investigate the sample morphology and materials composition after long-time stability test to rule out any effect of side reaction affecting the achievement of the long-term stability. The sample after the long cycling test of over 15 h was then investigated in detail using SEM imaging, XRD, and elemental mapping analyses as shown in Figure 4. The morphology of $CoFe_2O_4$ NPs on CFP does not change significantly (Figure 4, parts a and b) and all materials are preserved on the sample without any material transformation (Figure 4c–h). Note that the negligible shift (with the same degree) in all the diffraction peaks for the XRD pattern after the long cycling test (see Figure 4c) comes from the XRD machine. The achieved observation along with the long stability test of current density versus time clearly indicates that $CoFe_2O_4$ is a robust OER catalyst in alkaline electrolytes.

Another promising feature of the $CoFe_2O_4$ NPs on CFP is that they can also work as HER catalyst (Figure 5) making

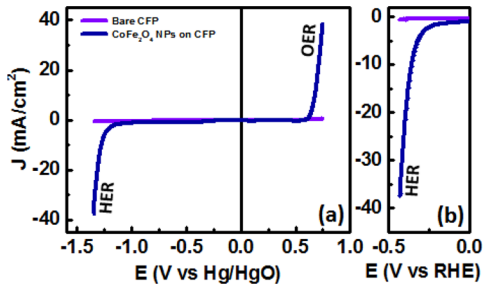

Figure 5. (a) Linear sweep voltammetry (LSV) measurement of $CoFe_2O_4$ NPs on CFP and bare CFP recorded at a scan rate of 20 mV/s in 1 M NaOH from positive to negative potentials. (b) Corresponding current density versus RHE for the HER performance. The plots are without any *iR* correction.

them a bifunctional electrocatalyst. As displayed in Figure 5a, the $CoFe_2O_4$ NPs-on-CFP electrode shows significantly enhanced OER and HER performances compared to bare CFP. The $CoFe_2O_4$ NPs-on-CFP electrode offers an HER current density of 10 mA/cm^2 at 356 mV overpotential (see the zoomed-in current density versus RHE for the HER in Figure 5b). As mentioned in the Experimental Section, we did not use any gas purging for the measurement in Figure 5. This was because we want to evaluate the suitability of the bifunctional catalyst for a full PEC system, consisting of semiconductor photocathode and photoanode, to handle overall spontaneous solar water splitting in one specific electrolyte and cell. Although the $CoFe_2O_4$ NPs-on-CFP electrode shows both HER and OER performances, it is more efficient for the OER due to low OER overpotential.

4. CONCLUSIONS

In summary, we showed $CoFe_2O_4$ NPs synthesized with a simple hydrothermal growth and their application on 3D CFPs for efficient and durable OER. The $CoFe_2O_4$ NPs on CFP exhibited orders of magnitude higher performance (current density, overpotential, and Tafel slope) than bare CFP, revealing the high activity of $CoFe_2O_4$ NPs for the OER. Significantly, the $CoFe_2O_4$ NPs-on-CFP sample showed long-term stability evaluated with 15 h of continuous cycling (>1000 cycles at a slow scan rate) and current density versus time for over 40 h without any morphological or compositional changes. Interestingly, the $CoFe_2O_4$ NPs-on-CFP electrodes also offered significantly enhanced HER performance compared to bare CFP, thus acting as a bifunctional catalyst. The obtained results reveal promising potential for efficient, cost-effective, and durable hydrogen production at large scales using earth-abundant materials with low-cost fabrication processes.

■ ASSOCIATED CONTENT

Supporting Information

The Supporting Information is available free of charge on the ACS Publications website at DOI: 10.1021/acsami.5b04270.

Additional images and plots (PDF)

■ AUTHOR INFORMATION

Corresponding Authors

*E-mail: jin@ucsd.edu (S.J.).
*E-mail: pbandaru@ucsd.edu (P.R.B.).

Notes

The authors declare no competing financial interest.

■ ACKNOWLEDGMENTS

This work was supported by the Iwama Endowed Fund at UCSD and the National Science Foundation (NSF CBET1236155). A.K. thanks Yong Jiang (Digi-Ivy, Inc.) and Siarhei Vishniakou (UCSD) for their help. A.K. also thanks Erick Martinez Loran (UCSD) for his assistance during the revision.

■ REFERENCES

(1) Walter, M. G.; Warren, E. L.; McKone, J. R.; Boettcher, S. W.; Mi, Q.; Santori, E. A.; Lewis, N. S. Solar Water Splitting Cells. *Chem. Rev.* **2010**, *110*, 6446–6473.

(2) Osterloh, F. E. Inorganic Nanostructures for Photoelectrochemical and Photocatalytic Water Splitting. *Chem. Soc. Rev.* **2013**, *42*, 2294–2320.

(3) Kim, D.; Sakimoto, K. K.; Hong, D.; Yang, P. Artificial Photosynthesis for Sustainable Fuel and Chemical Production. *Angew. Chem., Int. Ed.* **2015**, *54*, 3259–3266.

(4) Gratzel, M. Photoelectrochemical cells. *Nature* **2001**, *414*, 338–344.

(5) Wang, G.; Ling, Y.; Wang, H.; Xihong, L.; Li, Y. Chemically Modified Nanostructures for Photoelectrochemical Water Splitting. *J. Photochem. Photobiol., C* **2014**, *19*, 35–51.

(6) Chemelewski, W. D.; Lee, H.-C.; Lin, J.-F.; Bard, A. J.; Mullins, C. B. Amorphous FeOOH Oxygen Evolution Reaction Catalyst for Photoelectrochemical Water Splitting. *J. Am. Chem. Soc.* **2014**, *136*, 2843–2850.

(7) Trotochaud, L.; Ranney, J. K.; Williams, K. N.; Boettcher, S. W. Solution-Cast Metal Oxide Thin Film Electrocatalysts for Oxygen Evolution. *J. Am. Chem. Soc.* **2012**, *134*, 17253–17261.

(8) Gong, M.; Li, Y.; Wang, H.; Liang, Y.; Wu, J. Z.; Zhou, J.; Wang, J.; Regier, T.; Wei, F.; Dai, H. An Advanced Ni–Fe Layered Double Hydroxide Electrocatalyst for Water Oxidation. *J. Am. Chem. Soc.* **2013**, *135*, 8452–8455.

(9) Lu, Z.; Wang, H.; Kong, D.; Yan, K.; Hsu, P.-C.; Zheng, G.; Yao, H.; Liang, Z.; Sun, X.; Cui, Y. Electrochemical Tuning of Layered

Lithium Transition Metal Oxides for Improvement of Oxygen Evolution Reaction. *Nat. Commun.* **2014**, *5*, 4345.
(10) Esswein, A. J.; Surendranath, Y.; Reece, S. Y.; Nocera, D. G. Highly Active Cobalt Phosphate and Borate Based Oxygen Evolving Catalysts Operating in Neutral and Natural Waters. *Energy Environ. Sci.* **2011**, *4*, 499−504.
(11) Kanan, M. W.; Nocera, D. G. In Situ Formation of an Oxygen-Evolving Catalyst in Neutral Water Containing Phosphate and Co^{2+}. *Science* **2008**, *321*, 1072−1075.
(12) Lutterman, D. A.; Surendranath, Y.; Nocera, D. G. A Self-Healing Oxygen-Evolving Catalyst. *J. Am. Chem. Soc.* **2009**, *131*, 3838−3839.
(13) Surendranath, Y.; Dincă, M.; Nocera, D. G. Electrolyte-Dependent Electrosynthesis and Activity of Cobalt-Based Water Oxidation Catalysts. *J. Am. Chem. Soc.* **2009**, *131*, 2615−2620.
(14) Liang, Y.; Li, Y.; Wang, H.; Zhou, J.; Wang, J.; Regier, T.; Dai, H. Co_3O_4 Nanocrystals on Graphene as a Synergistic Catalyst for Oxygen Reduction Reaction. *Nat. Mater.* **2011**, *10*, 780−786.
(15) McCrory, C. C. L.; Jung, S.; Peters, J. C.; Jaramillo, T. F. Benchmarking Heterogeneous Electrocatalysts for the Oxygen Evolution Reaction. *J. Am. Chem. Soc.* **2013**, *135*, 16977−16987.
(16) Yang, Y.; Fei, H.; Ruan, G.; Xiang, C.; Tour, J. M. Efficient Electrocatalytic Oxygen Evolution on Amorphous Nickel−Cobalt Binary Oxide Nanoporous Layers. *ACS Nano* **2014**, *8*, 9518−9523.
(17) Deng, X.; Tüysüz, H. Cobalt-Oxide-Based Materials as Water Oxidation Catalyst: Recent Progress and Challenges. *ACS Catal.* **2014**, *4*, 3701−3714.
(18) Suntivich, J.; May, K. J.; Gasteiger, H. A.; Goodenough, J. B.; Shao-Horn, Y. A Perovskite Oxide Optimized for Oxygen Evolution Catalysis from Molecular Orbital Principles. *Science* **2011**, *334*, 1383−1385.
(19) Reece, S. Y.; Hamel, J. A.; Sung, K.; Jarvi, T. D.; Esswein, A. J.; Pijpers, J. J. H.; Nocera, D. G. Wireless Solar Water Splitting Using Silicon-Based Semiconductors and Earth-Abundant Catalysts. *Science* **2011**, *334*, 645−648.
(20) Yang, J.; Walczak, K.; Anzenberg, E.; Toma, F. M.; Yuan, G.; Beeman, J.; Schwartzberg, A.; Lin, Y.; Hettick, M.; Javey, A.; Ager, J. W.; Yano, J.; Frei, H.; Sharp, I. D. Efficient and Sustained Photoelectrochemical Water Oxidation by Cobalt Oxide/Silicon Photoanodes with Nanotextured Interfaces. *J. Am. Chem. Soc.* **2014**, *136*, 6191−6194.
(21) Liao, M.; Feng, J.; Luo, W.; Wang, Z.; Zhang, J.; Li, Z.; Yu, T.; Zou, Z. Co_3O_4 Nanoparticles as Robust Water Oxidation Catalysts Towards Remarkably Enhanced Photostability of a Ta_3N_5 Photoanode. *Adv. Funct. Mater.* **2012**, *22*, 3066−3074.
(22) Singh, R. N.; Singh, N. K.; Singh, J. P.; Balaji, G.; Gajbhiye, N. S. Effect of Partial Substitution of Cr on Electrocatalytic Properties of $CoFe_2O_4$ Towards O_2-Evolution in Alkaline Medium. *Int. J. Hydrogen Energy* **2006**, *31*, 701−707.
(23) Indra, A.; Menezes, P. W.; Sahraie, N. R.; Bergmann, A.; Das, C.; Tallarida, M.; Schmeißer, D.; Strasser, P.; Driess, M. Unification of Catalytic Water Oxidation and Oxygen Reduction Reactions: Amorphous Beat Crystalline Cobalt Iron Oxides. *J. Am. Chem. Soc.* **2014**, *136*, 17530−17536.
(24) Bian, W.; Yang, Z.; Strasser, P.; Yang, R. A $CoFe_2O_4$/Graphene Nanohybrid as an Efficient Bi-Functional Electrocatalyst for Oxygen Reduction and Oxygen Evolution. *J. Power Sources* **2014**, *250*, 196−203.
(25) Liu, S.; Bian, W.; Yang, Z.; Tian, J.; Jin, C.; Shen, M.; Zhou, Z.; Yang, R. A Facile Synthesis of $CoFe_2O_4$/Biocarbon Nanocomposites as Efficient Bi-functional Electrocatalysts for the Oxygen Reduction and Oxygen Evolution Reaction. *J. Mater. Chem. A* **2014**, *2*, 18012−18017.

DOI: 10.1021/acsami.5b04270
ACS Appl. Mater. Interfaces 2015, 7, 17851−17856